Cu_2O@CoO Yolk-Shell Hierarchical Structures for High-Efficient Cascade Electrocatalytic Nitrate Reduction to Ammonia

Wenjing Huang, Wenyu Luo, Jiawei Liu, Bei-Er Jia, Carmen Lee, Jinfeng Dong, Lan Yang, Bin Liu and Qingyu Yan**

Wenjing Huang — Guangzhou Key Laboratory of Low-Dimensional Materials and Energy Storage Devices, Collaborative Innovation Center of Advanced Energy Materials, School of Materials and Energy, Guangdong University of Technology, Guangzhou 510006, China; School of Materials Science and Engineering, Nanyang Technological University, Singapore 639798, Singapore

Wenyu Luo — School of Materials Science and Engineering, Nanyang Technological University, Singapore 639798, Singapore

Jiawei Liu — School of Materials Science and Engineering, Nanyang Technological University, Singapore 639798, Singapore

Bei-Er Jia — School of Materials Science and Engineering, Nanyang Technological University, Singapore 639798, Singapore

Carmen Lee ― School of Materials Science and Engineering, Nanyang Technological University, Singapore 639798, Singapore

Jinfeng Dong ― School of Materials Science and Engineering, Nanyang Technological University, Singapore 639798, Singapore

Lan Yang ― School of Materials Science and Engineering, Nanyang Technological University, Singapore 639798, Singapore

Bin Liu ― Department of Materials Science and Engineering, City University of Hong Kong, Hong Kong SAR 999077, China; Email: bliu48@cityu.edu.hk (B.L.)

Qingyu Yan ― School of Materials Science and Engineering, Nanyang Technological University, Singapore 639798, Singapore; Email: alexyan@ntu.edu.sg (Q.Y.)

* Corresponding Authors

KEYWORDS: Nitrate reduction reaction, Ammonia synthesis, Yolk-shell nanostructure, Cascade electrocatalysis, Membrane electrode assembly (MEA)

ABSTRACT: Electroreduction of nitrate to ammonia *via* a selective eight-electron transfer nitrate reduction reaction offers a promising, low energy consumption, pollution-free, green NH_3 synthesis strategy alternative to the Haber-Bosch method. However, it remains a great challenge to achieve high NH_4^+ selectivity and complete conversion from NO_3^--N to NH_4^+-N. Herein, we report ingredients adjustable Cu_2O@CoO yolk-shell nanocubes feature with tunable inner void

spaces and diverse activity centers, favoring rapid cascade conversion of NO_3^- to NO_2^- on Cu_2O and NO_2^- to NH_4^+ on CoO. Cu_2O@CoO yolk-shell nanocubes exhibit super NH_4^+ Faradaic efficiencies (> 99 %) over a wide potential window (-0.2 V to -0.9 V *vs*. RHE), with considerable NH_4^+ yield rate of 15.27 mg h^{-1} cm^{-2} and fantastic cycling stability and long-term chronoamperometric durability. Cu_2O@CoO yolk-shell nanocubes exhibited glorious NO_3^--N to NH_4^+-N conversion efficiency (CE) in both dilute (500 ppm) and highly concentrated (0.1 M and 1 M) NO_3^- electrolytes, respectively. The nitrate electrolysis membrane electrode assembly (MEA) system equipped with Cu_2O@CoO yolk-shell nanocubes delivers over 99.8% NH_4^+ Faradaic efficiency at cell voltages of 1.9 V to 2.3 V.

INTRODUCTION

Ammonia (NH_3) is well known as the most critical chemical in agriculture, industry and national defense as well as an excellent carbon-free energy carrier (4.32 kWh L^{-1}).[1, 2] Up to now, industrial ammonia synthesis mainly relies on energy and CO_2 emission intensive Haber-Bosch process invented more than a hundred years ago. Industrial NH_3 production from Haber-Bosch process accounts for ~2% of global energy consumption and emits 300 million tons of CO_2 per year, climbing further.[3-5] Green electrochemical ammonia synthesis technology driven by renewable electricity offers one of the most promising alternatives to alleviate the energy crisis and severe carbon emission problems. However, electrochemical N_2 reduction reaction (NRR) for NH_3 production suffers from the ultra-low N_2 solubility in aqueous solution and high energy barrier of cleaving N≡N bond (941 kJ mol^{-1}). The NH_3 yield rate of NRR is two to three orders of magnitude lower than that of the Haber-Bosch method.[6-8] Moreover, rising NO_3^- levels induced by the excessive usage of NH_3 and its further nitrification process, causes serious environmental and health problems, disturbing the balance of global nitrogen cycle.[9-13] Recently, electrochemical

nitrate reduction to ammonia has attracted growing research interests for both nitrate removal from wastewater and green NH_3 production. However, nitrate reduction to NH_3 is complex involving nine-proton coupled with eight-electron transfer, competing with hydrogen evolution reaction (HER) and other by-products (such as NO_2^-, N_2, NH_2OH).[13, 14] For complex multi-electron transfer proton coupling reactions (such as NO_3^-RR), designing well-defined special hierarchical structures with various active sites is pivotal for the highly efficient conversion of NO_3^- to NH_4^+. Yet, it currently still suffers from insignificant attention.

Yolk-shell structures, featuring adjustable inner void and flexible manipulation of shell, yolk, and void, have received immense attention in energy storage, sensing, and catalysis.[15-18] The inner void of yolk-shell nanomaterials provides large spaces for the occurrence of mass transfer and catalysis. While the adjustable shell, yolk, and void structure can supply diversified active sites, facilitating adsorption and conversion of different intermediates. Very recently, Cu_2O species demonstrated remarkable NO_3^- to NO_2^- two-electron conversion activity.[19-21] Co and its derivatives are proposed great applications in electrosynthesis ammonia from nitrate/nitrite.[22-25] Yet, Co and its derivatives normally undergo ultra-high energy barrier to achieve NO_3^--to-NO_2^- conversion before the following conversion of NO_2^- to NH_4^+, demanding very negative applied potentials.[23] Yolk-shell nanomaterials with synergistic action between a variety of components of yolk-shell nanomaterials are conducive to break down the sequential reaction steps, optimizing active sites for electrochemical conversion of NO_3^- to NH_4^+.

Inspired by these early works, herein, we constructed Cu_2O@CoO yolk-shell nanocubes with elastic inner void spaces and chemical components, revealing excellent electrochemical nitrate reduction to NH_3 performance in both dilute and highly concentrated NO_3^- electrolytes. Cu_2O@CoO nanocubes achieved NH_3 Faradaic efficiencies (FE) of over 99 % at the potential

window from -0.2 to -0.9 V *vs*. RHE, with a maximum NH_3 yield of ~15.27 mg h^{-1} cm^{-2} at -0.9 V *vs*. RHE, comparable to traditional Haber-Bosch ammonia synthesis process. Cu_2O@CoO nanocubes possessed excellent operating cycling stability and long-term durability as well. Furthermore, Cu_2O@CoO nanocubes displayed glorious NO_3^--N to NH_4^+-N conversion efficiency in both diluted and concentrated NO_3^- media, respectively. Electrochemical kinetics analysis revealed that Cu_2O@CoO yolk-shell nanocubes possess the optimized k_1 and k_2 values for rapid consequent conversion of NO_3^- to NO_2^- and NO_2^- to NH_4^+ owing to the favorable yolk-shell hierarchical structures and reasonable chemical composition. To demonstrate practical application potentials, the Cu_2O@CoO yolk-shell nanocubes were used to construct the membrane electrode assembly. The nitrate electrolysis cell with the Cu_2O@CoO yolk-shell nanocube cathode could reach 99.9 % NH_3 FE at cell voltages from 1.9 V to 2.3 V and achieve a maximum NH_3 yield rate of 31.50 mg h^{-1} cm^{-2}. This work paves a new insight into the design of high-performance nitrate reduction to ammonia electrocatalysts and provides a promising green NH_3 production alternative for the Haber-Bosch method.

RESULTS AND DISCUSSION

Cu_2O@CoO yolk-shell nanocubes were prepared by a facile two-step solution method under ambient conditions. In the first step, Cu_2O nanocubes were synthesized in the presence of trisodium citrate at room temperature. The as-synthesized Cu_2O displays nanocube structure with an average size of ~260 nm (Figure. S1). The harvested Cu_2O nanocubes were re-dispersed in a mixed solution of deionized water and ethanol containing $CoCl_2$ precursor and polyvinyl pyrrolidone (PVP), followed by adding $Na_2S_2O_3$ etchant for coordinating etching and precipitating (CEP).[26] During this process, Cu_2O was etched by $S_2O_3^{2-}$, generating a large amount of OH^- near the nanocube surface. Free Co^{2+} ions were precipitated synchronously, forming the shell structure

around the Cu_2O surface. CoO nanosheet shell was finally formed after heat treatment in vacuum. We successfully obtained various ratios of Cu_2O : CoO in the yolk-shell nanocubes by adjusting the amount of added $Na_2S_2O_3$ (Figure. S2). The best Cu_2O@CoO yolk-shell nanocube structure was verified to contain 38.5 wt.% of CoO and 61.5 wt.% of Cu_2O from the inductively coupled plasma emission spectroscopy (ICP) analysis, named as Cu_2O@CoO. The CoO and Cu_2O components of other ratios in the Cu_2O@CoO yolk-shell nanocubes are summarized in Table S1.

X-ray diffraction (XRD) was carried out to identify the crystalline phase of the Cu_2O@CoO yolk-shell nanocubes. The first product displays diffraction peaks that match well with the cubic Pn-3m crystal phase of Cu_2O (JCPDS No. 74-1230) without any other detectable impurity diffraction peaks (Figure. S3a), which can be further confirmed by the selected area electron diffraction (SAED) pattern as shown in Figure. S3b. After CEP process and the subsequent heat treatment in vacuum, the XRD pattern of final product exhibits both diffraction peaks of Cu_2O and CoO. The diffraction peaks located at 29.69˚, 36.57˚, 42.48˚, 52.68˚, 61.62˚, 73.84˚, and 77.34˚ belong to Cu_2O (JCPDS No. 74-1230), while the diffraction peak at 34.10˚ can be assigned to CoO (JCPDS No. 75-0419) (Figure. S4). Compared to Cu_2O, the diffraction peak intensity of CoO is much lower. The diffraction peaks of Cu_2O become weaker with increasing addition amount of $Na_2S_2O_3$. As shown in Figure. 1a, it can be observed that plentiful of ultrathin CoO nanosheets are randomly decorated on the surface of Cu_2O. The solid irregularly shaped Cu_2O distributes in the inner core. High-resolution transmission electron microscopy (HR-TEM) measurements reveal clear lattice fringes from the (220) and (111) planes of CoO nanosheets (Figure. 1b). In contrast, it is not easy to identify the inner Cu_2O lattice fringes using HR-TEM under the same measurement conditions. The SAED pattern exhibits apparent diffraction rings of (111) and (220) planes from CoO, while the diffraction spots of (111) and (110) belong to Cu_2O, demonstrating the

polycrystalline nature of the CoO shell and single crystal core structure of Cu_2O (Figure. 1c). Energy dispersive X-ray spectroscopy (EDS) line scans as displayed in Figure. 1d and 1e indicate that the shell is indeed rich in Co element, whereas Cu element is only detectable in the inner core. Moreover, the spatial distribution of Cu and Co elements match well with their physical positions observed in STEM (Figures. 1f-1i). These experimental data confirm that the yolk-shell Cu_2O@CoO nanocubes contain a CoO-rich shell and a Cu_2O-rich core.

X-ray photoelectron spectroscopy (XPS) was performed to investigate the valence states of the as-synthesized Cu_2O@CoO yolk-shell nanocubes. Figure. S5 shows the survey XPS spectrum, in which no impurity elements can be detected, in accordance with the XRD and EDS mapping results. As shown in the Co 2p XPS spectrum (Figure. 2a), the Co peaks at the binding energy of 780 eV and 795.9 eV with intense satellites can be assigned to Co $2p_{1/2}$ and Co $2p_{3/2}$ of CoO. The strong satellites originate from the charge transfer band structure found in late *3d* transition metal monoxide with partially filled e_g character,[27] which are often used to distinguish CoO from Co_3O_4. The O 1s XPS spectrum can be deconvoluted into O from surface hydroxyl groups, Co-O bonds and Cu-O bonds, respectively (Figure. 2b). According to the Cu LMM spectrum (Figure 2c), Cu_2O@CoO yolk-shell nanocubes were predominant with Cu^+ with a tiny amount of Cu^{2+}. The Cu^{2+} species might probably originate from the oxidation of Cu^+ by oxygen in the air, which is common in nanomaterials. Raman spectroscopy measurements were further conducted to study the chemical components of the as-prepared electrocatalysts. As shown in Figure. 2d, Cu_2O nanocubes display an inactive Raman mode Γ_{12}^- and an infrared mode $\Gamma_{15}^{-(1)}$(LO) at the Raman shift of 109 and 149 cm^{-1}, respectively. The most intense Raman shift of Cu_2O at 220 cm^{-1} refers to the second order overtone of Cu_2O. Other two broad Raman modes at 416 and 629 cm^{-1} can be assigned to one fourth order overtone $4\Gamma_{12}^-$ and one red allowed mode $\Gamma_{15}^{-(2)}$ (TO).[28] As for CoO

nanosheets, there are discernible E_g, F_{2g}, and A_{1g} peaks, belonging to the CoO phase.[29-31] The as-prepared Cu_2O@CoO yolk-shell nanocubes display both characteristic Raman modes of Cu_2O and CoO.

The electrochemical performance of Cu_2O@CoO yolk-shell nanocubes, Cu_2O nanocubes and CoO nanosheets for nitrate reduction reaction was measured in a standard H-cell. The amounts of NO_3^- and NO_2^- product were quantified by ion chromatography (Figure. S6 and Figure. S7), and the NH_4^+ product was determined by the indophenol blue method (Figure. S8). Linear sweep voltammetry measurement was first carried out in 1 M KOH electrolyte with and without 0.1 M KNO_3 (Figure. 3a and Figure. S9). Cu_2O@CoO yolk-shell nanocubes, Cu_2O nanocubes and CoO nanosheets exhibit evidently enlarged current density at the same applied cathodic potential in the presence of NO_3^- (Figure. 3a and Figure. S9), which is attributed to NO_3^- reduction reaction (NO_3^- RR). The chronopotentiometric measurement was applied to investigate the potential-dependent product selectivity of nitrate reduction reaction (Figure. S10). As shown in Figure. 3b, Cu_2O@CoO yolk-shell nanocubes present an NH_4^+ Faradaic efficiency (FE) of 98.7 % at -0.1 V *vs*. RHE and keep a stable NH_4^+ FE over 99% across a broad potential widow from -0.2 V to -0.9 V *vs*. RHE. The yield rate of NH_4^+ gradually increases from 0.192 mg h^{-1} cm^{-2} at -0.2 V *vs*. RHE to 15.27 mg h^{-1} cm^{-2} at -0.9 V *vs*. RHE, with a maximum NH_4^+ partial current density up to ~230 mA cm^{-2} (Figure. 3c). Additionally, Cu_2O@CoO yolk-shell nanocubes were carried out in 1 M KOH without and without NO_3^-, and the NH_4^+ products were quantified by IC and UV-Visibel spectrophotometer. There were no detachable NH_4^+ products measured in the electrolyte without NO_3^-. Concurrently, the NH_4^+ concentrations of Cu_2O@CoO yolk-shell nanocubes collected at -0.2 V and -0.8 V reach up to 7.9 mg L^{-1} and 247.4 mg L^{-1} (Figure S11), respectively, according to both IC and UV-Visibel spectrophotometer results. In sharp contrast, Cu_2O nanocubes favor

converting NO_3^- to NO_2^-, especially at less negative potentials (Figure. S12), with a NO_2^- FE as high as 96.05 % at 0 V *vs*. RHE. The nitrate reduction reaction over CoO nanosheets starts at a more negative applied potential (Figure. S9b), compared to Cu_2O nanocubes and Cu_2O@CoO yolk-shell nanocubes, implying that pure CoO has to overcome a much larger energy barrier to realize NO_3^- reduction reaction. NH_4^+ is a more preferred nitrate reduction product over CoO nanosheets, different from NO_2^- over Cu_2O nanocubes (Figure. S13).

To investigate how composition of Cu_2O@CoO yolk-shell nanocubes influenced the nitrate reduction reaction, we prepared Cu_2O@CoO yolk-shell nanocubes with different Cu_2O to CoO ratios by adjusting the amount of the added $Na_2S_2O_3$ etchant (donated as Cu_2O@CoO-1 and Cu_2O@CoO-2). Among which, the Cu_2O@CoO yolk-shell nanocubes with a Cu_2O/CoO molar ratio of 1.5:1 possess the best nitrate reduction to ammonia performance (Figure. S14 and Figure. 15), which is among the best electrocatalysts reported in the literature for nitrate reduction reaction (Table S2). On the other hand, physical mixture of Cu_2O nanocubes and CoO nanosheets displayed much inferior NO_3^--to-NH_4^+ reduction performance as compared to the Cu_2O@CoO yolk-shell nanocubes with the same Cu_2O/CoO molar ratio (Figure. S16). Therefore, it is reasonably inferred that the brilliant electrochemical nitrate reduction to ammonia performance over Cu_2O@CoO yolk-shell nanocubes can be assignable to the distinctive yolk-shell hierarchical structures and reasonable chemical composition.

Long-term cycling and chronopotentiometric durability of Cu_2O@CoO yolk-shell nanocubes for NO_3^-RR were assessed. As presented in Figure. 3d, Figures. S17 and S18, Cu_2O@CoO yolk-shell nanocubes can maintain stable NH_4^+ FE and yield rate during 24 h of cyclic measurements at both -0.2 V and -0.8 V *vs*. RHE. For continuous chronopotentiometric measurement (Figure. S19) without changing electrolyte, Cu_2O@CoO yolk-shell nanocubes appear an evident decrease

of current density over time (Figure. S19), due to consumption of NO_3^- in the electrolyte. After less than 18 h of continuous reaction, NO_3^- can be exclusively converted to NH_4^+, achieving 100 % conversion from NO_3^--N to NH_4^+-N (Figure. 3e). To study the intrinsic catalytic stability of Cu_2O@CoO yolk-shell nanocubes, we adopted a flow electrolyte H-cell configuration, keeping stable NO_3^- concentration. Over 48 h of chronopotentiometric measurement, Cu_2O@CoO yolk-shell nanocubes could deliver stable current density with near unit NH_4^+ FE at -0.8 V *vs*. RHE (Figure. 3f).

In real water environments, the NO_3^- concentration of nitrate-containing surface wastewater is much lower than that in laboratory research. Therefore, it is necessary to explore the electrocatalytic performance of Cu_2O@CoO yolk-shell nanocubes at low nitrate concentrations. Cu_2O@CoO yolk-shell nanocubes were further performed in 1 M KOH + 500 ppm NO_3^-. The NH_4^+ FE of Cu_2O@CoO yolk-shell nanocubes increased from 61.7% at -0.1 V *vs*. RHE to 98.7% at -0.2 V *vs*. RHE, and decreased with the increasing negative applied potentials (Figure S20). It is well accepted that hydrogen evolution reaction (HER) was the main competitive reaction of electrochemical NO_3^-RR. The decreased NH_4^+ FE of Cu_2O@CoO yolk-shell nanocubes in low NO_3^- concentration would be assigned to the insufficient NO_3^- supply in the electrolyte. HER showed an enhanced activity while applying negative potentials, resulting in reduced NH_4^+ FEs. Cu_2O@CoO yolk-shell nanocubes were further measured at -0.8 V in 1 M KOH with 500 ppm NO_3^-. Cu_2O@CoO yolk-shell nanocubes demonstrated a NO_3^- to NH_4^+ conversion efficiency of 99.76% (Figure S21), demonstrating important application potential in low-concentration NO_3^- conversion. The final concentration of NO_3^- was 0.8 mg L^{-1}, much lower than the recommended maximum contaminant levels of the World Health Organization (< 10 mg L^{-1} for NO_3^-),[2] demonstrating great potential for real-world applications.

In actual industrial operation, the NO_3^--containing wastewater would be pretreated to highly concentrated NO_3^- wastewater before further denitrification treatment. To assess the industrial application potential, we employed Cu_2O@CoO yolk-shell nanocubes for nitrate reduction in 1.0 M NO_3^- in presence of 1 M KOH. Ion chromatography real-time monitoring of NO_3^- combined with real-time NH_4^+ quantification shows that 1 M of NO_3^- can be completely converted into ~0.92 M of NH_4^+ (Figure. 3g). The slightly lower NH_4^+ concentration than the stoichiometric concentration of NO_3^- is due to the volatility of ammonia, and some ammonia escaped from the electrolyte to the atmosphere. Additionally, we also assessed the NO_3^-RR performance of Cu_2O@CoO yolk-shell nanocubes in KOH with increasing NO_3^- concentration from 100 ppm to 0.5 M (Figure. S22). The NH_4^+ FEs of Cu_2O@CoO yolk-shell nanocubes keep around 99 % in various electrolytes with low to high NO_3^- concentrations (Figure. 3h), demonstrating the significant electrochemical NO_3^--to-NH_4^+ conversion performance over Cu_2O@CoO yolk-shell nanocubes.

We first tried to perform *in-situ* Raman spectroscopy to real active phases of Cu_2O@CoO for electrochemical nitrate reduction. Only Cu_2O and CoO Raman modes were detectable over Cu_2O@CoO yolk-shell nanocubes during the NO_3^-RR cyclic voltammetry measurement process (Figures. S23, S24 and Figures. 4a, 4b). According to recent research work, oxidized Cu-based materials usually undergo structural or chemical evolution under reduction conditions over time. We further explored the morphology, chemical composition, and oxidation state of Cu_2O@CoO yolk-shell nanocubes after a 24-hour long-term measurement. Cu_2O@CoO electrocatalysts remained stable yolk-shell hierarchical structures after long-term stability measurements (Figure S25). According to the XRD pattern (Figure S26), Cu_2O@CoO yolk-shell structures consisted of mixed phases of $Co(OH)_2$, CuO, Cu_2O, and Cu after a long-term stability measurement. Besides,

the obvious Cu-O Raman mode of CuO and the formation mode of β-$Co(OH)_2$ were detected in further Raman analysis (Figure S27). The D band and G band located at 1340 cm^{-1} and ~1592 cm^{-1}, respectively, would be assigned to the carbon fiber paper. We also performed XPS to explore the oxidation state of Cu_2O@CoO yolk-shell nanocubes after long-term measurement (Figure S28). As shown in the high-resolution Co 2p XPS (Figure S28a), the convolution peaks located at 780.6 eV and 796.4 eV were assigned to Co $2p_{1/2}$ and Co $2p_{3/2}$ of $Co(OH)_2$.[32] And the Cu_2O@CoO yolk-shell nanocubes after long-term measurement appeared in Cu^{2+}, Cu^{+}, and Cu^{0} oxidation states (Figure S28b and S28c). Together with these experimental results, we suggested that the chemical evolution of Cu_2O@CoO yolk-shell nanocubes during the NO_3^-RR process is slow. Therefore, no obvious $Co(OH)_2$ and Cu derivatives signals were detected in the *in-situ* Raman spectra collected during CV measurements. Besides, the Cu^{2+} existence of Cu_2O@CoO yolk-shell hierarchical structures after long-term reduction measurements might be attributed to highly oxidative nitrogen dioxide (NO_2) intermediates generated during the NO_3^-RR process.[19, 20] Thence, the advantageous electrosynthesis of ammonia performance of the Cu_2O@CoO yolk-shell hierarchical structures would give credit from the mixed phases of $Co(OH)_2$, Cu_2O, CuO, and Cu metal.

According to previous research, electrochemical nitrate reduction to ammonia follows a series of deoxidation ($* NO_3^- \rightarrow * NO_2 \rightarrow * NO \rightarrow * N$) and hydrogenation ($* N \rightarrow * NH \rightarrow * NH_2 \rightarrow * NH_3$) steps,[33, 34] and the first deoxidation step from *NO_3 to *NO_2 is well accepted as the rate-determining step. The distinctive Cu_2O@CoO yolk-shell nanocube structure is ideal for the cascade electrochemical reduction of *NO_3^- to *NO_2^- and *NO_2^- to NH_4^+ with flexible inner voids for rapid mass transport and diverse active centers for catalysis. Pure Cu_2O nanocubes appeared NO_2^- FEs over 50% at the potential window of 0 ~ -0.3 V *vs*. RHE, reaching high up to ~98% (Figure S11). Besides, Cu_2O nanocubes showed an overpotential of 0.091 V *vs*. RHE to reach 10

mA cm^{-2} in 1 M KOH + 0.1 M KNO_3, much positive than that of in 1 M KOH + 0.1 M KNO_2 (-0.017 V *vs*. RHE) (Figure S29). These suggested that Cu_2O nanocubes favor to convert NO_3^- to NO_2^-. Reversely, CoO nanosheets revealed an overpotential (10 mA cm^{-2}) of -0.27 V in 1 M KOH + 0.1 M KNO_2, much more positive than that in 1 M KOH + 0.1 M KNO_3 (-0.33 V *vs*. RHE) (Figure 4c). CoO nanosheets are more active for $*NO_2^-$-to-NH_4^+ conversion than $*NO_3^-$-to-$*NO_2^-$ (Figure. 4c*)*, which display obviously enhanced NH_4^+ selectivity in the presence of KNO_2 than KNO_3 (Figure. 4d). We further calculated the rate constants for NO_3^- electrocution (k_1) and NO_2^- electroreduction (k_2) to get more insight into the cascade synergetic role of Cu_2O and CoO during the electrochemical conversion of NO_3^- to NH_4^+. The larger k_1/k_2 values indicate faster electrochemical conversion processes of NO_3^- to NO_2^- or NO_2^- to NH_4^+.[35] Among them, pure Cu_2O possessed the largest k_1 value and smallest k_2 value (Figure S30). Concurrently, pure CoO accounted for the smallest k_1 value and largest k_2 value. In sharp contrast, Cu_2O@CoO yolk-shell nanocubes possessed both the optimized k_1 and k_2 values. manifesting successively rapid conversions of NO_3^- to NO_2^- and NO_2^- to NH_4^+ on Cu_2O@CoO yolk-shell hierarchical structures with the assistance of the synergetic promotion of Cu_2O and CoO. Besides, Cu_2O nanocubes and Cu_2O@CoO yolk-shell nanocubes display a Tafel slope of 110 and 116 mV dec^{-1} in 1 M KOH +0.1 M KNO_3 (Figure. 4e), respectively, implying that the first electron transfer during NO_3^--to-NO_2^- deoxidation is the RDS of NO_3^-RR.[36-38] On the other hand, CoO nanosheets show a much higher Tafel slope of 148 mV dec^{-1}, indicating limitation of initial adsorption and activation of NO_3^- during the NO_3^-RR process.[37] In 0.1 M KNO_2 + 1 M KOH electrolyte (Figure. 4f), CoO nanosheets and Cu_2O@CoO yolk-shell nanocubes display a Tafel slope of 90 mV dec^{-1} and 109 mV dec^{-1}, respectively, suggesting that the first electron transfer from $*NO_2^-$ to NO conversion is the RDS.[36, 37] Cu_2O nanocubes show a Tafel slope of 66 mV dec^{-1} in 0.1 M KNO_2 + 1 M KOH

electrolyte, indicating that the RDS is the chemical step.[39, 40] Based on the electrokinetic analysis results, the brilliant NO_3^-RR performance on Cu_2O@CoO yolk-shell nanocubes can be attributed to the efficient cascade synergetic promotion role of their hierarchical structure and reasonable chemical composition.

To demonstrate the industrial application potential of NO_3^-RR, we fabricated a two-electrode membrane-electrode assembly (MEA) electrolysis cell equipped with a Cu_2O@CoO yolk-shell nanocube cathode and an IrO_2 anode (Figure 5). The anion exchange membrane was applied to separate the cathode and anode. The anodic and cathodic electrolytes went through MEA at a flow rate of 80 sccm with the assistance of a peristaltic pump. As shown in Figure 5b, the MEA equipped with Cu_2O@CoO yolk-shell nanocubes reached 10 mA cm^{-2} and 100 mA cm^{-2} at the cell voltages of 1.78 V and 2.02 V without *iR* compensation, respectively. Moreover, it is able to deliver an industry-relevant current density of 375 mA cm^{-2} at a small cell voltage of 2.3 V (Figure. 5b). We further assessed the electrosynthesis ammonia performance of MEA at the cell window of 1.9 V to 2.3 V. The MEA displayed NH_4^+ FEs over 99.85% from 1.9 V to 2.3 V, and the corresponding NH_4^+ yield rate increased from 6.82 mg h^{-1} cm^{-2} to 31.50 mg h^{-1} cm^{-2} (Figure. 5c).

CONCLUSION

In summary, we have successfully constructed Cu_2O@CoO yolk-shell nanocubes for cascade electrochemical nitrate reduction to NH_4^+, which exhibit excellent NO_3^-RR performance with NH_4^+ Faradaic efficiencies greater than 99 % across a wide potential window from -0.2 V to -0.9 V *vs*. RHE, considerable NH_4^+ yield rate of 15.27 mg h^{-1} cm^{-2} and fantastic cycling stability and long-term chronoamperometric durability. Cu_2O@CoO yolk-shell nanocubes displayed a 99.76%, 100%, and 92% conversion efficiency of NO_3^--N to NH_4^+-N in diluted (500 ppm) and highly concentrated (0.1 M and 1 M) NO_3^- electrolytes. Experimental results demonstrate that the

excellent NO_3^-RR performance of the Cu_2O@CoO yolk-shell nanocubes originates from the efficient cascade synergetic promotion role of their hierarchical structure and reasonable chemical composition. The Cu_2O@CoO yolk-shell nanocubes show industrial application potential to drive NO_3^-RR in an MEA electrolysis cell with a maximum NH_4^+ yield rate of 31.50 mg h^{-1} cm^{-2}.

MATERIALS AND METHODS

Preparation of Cu_2O nanocubes: In a typical synthesis, 1 mmol $CuSO_4$•5 H_2O and 0.5 mmol trisodium citrate dissolved in 80 mL DI water (18.2 Ω). 1.25 mol L^{-1} (10 mL) of NaOH solution was added into the above solution drop by drop under magnetic stirring for 5 min. The color of the solution changed from transparent light blue to dark blue suspension. Next, 10 mL of 1.5 mmol L-ascorbic acid (AA) aqueous solution was added to the above dark blue suspension under magnetic stirring for another 15 min. The color of the solution changed to yellow and brick red in sequence. The above solution was left at room temperature for 2 hours, washing with DI water and ethanol several times, respectively. The precipitates were dried under vacuum conditions at 80 ºC overnight.

Preparation of Cu_2O@CoO yolk-shell nanocubes: Different ratios of Cu_2O@CoO yolk-shell nanocubes were synthesized by adjusting the additional amount of $Na_2S_2O_3$ coordinating etchant. Taking Cu_2O@CoO as an example, 66 mg of Cu_2O nanocubes were dispersed in 80 mL DI water (18.2 Ω). 44 mg of $CoCl_2$ and 1.3 g polyvinyl pyrrolidone (PVP, Mw = 55000) were dispersed in 80 mL ethanol. These two solutions were mixed together under vigorous magnetic stirring. 3 g of $Na_2S_2O_3$ were dissolved in 50 mL of DI water. The $Na_2S_2O_3$ solution was dropped into the above mix solution under magnetic stirring. And the color changes from orange to light green. Then, the light green solution was left at room temperature for 1 hour, further separating impurities by centrifugation using deionized water and ethanol several times. The Cu_2O@CoO yolk-shell

nanocube reactor was finally dried overnight in a vacuum oven at 80 ℃. Cu_2O@CoO-1 and Cu_2O@CoO-2 yolk-shell nanocubes were prepared with the additional $Na_2S_2O_3$ amounts of 0.5 g and 5g, respectively.

Preparation of CoO nanosheets: 44 mg $CoCl_2$ were dispersed in 80 mL DI water and 80 mL ethanol containing 1.3 g of PVP (Mw = 55000) under vigorous magnetic stirring. 50 mL $Na_2S_2O_3$ (0.4 mol L^{-1}) aqueous solution dropped into the above solution under magnetic stirring for~10 min. After 1 h reaction at room temperature, the precipitates were collected by centrifugation with DI water and ethanol, and dried overnight in a vacuum oven at 80 ℃.

Electrochemical measurements of nitrate reduction to ammonia: All electrochemical results were collected in a multi-channel Solartron electrochemical workstation with a standard three-electrode system in a standard H-cell. A proton exchange membrane (Dupont nafion membrane 117) separated the anode and cathode sides. A Pt mesh electrode (1 cm×1 cm) and a Hg/HgO electrode acted as counter and reference electrodes, respectively. Electrocatalyst-loaded carbon fiber paper (Toray TGPH060) with a size of 1 cm×1 cm is the working electrode. Electrocatalyst ink was prepared as follows: 1 mg of electrocatalysts and 0.3 mg carbon black (as the conductive additive) were dispersed in the mixture of ethanol and DI water ($V_{ethanol}/V_{DI\ water}$ = 1/1), added with 10 μL 5 wt.% Nafion solution. The uniform electrocatalyst ink was obtained after vigorously sonicated treatment for 30 min. Subsequently, 100 μL of electrocatalyst ink was drop-cast on the carbon fiber paper and dried naturally. Before nitrate reduction reaction measurement, electrocatalysts were first activated in 1 M KOH by CV cycling at the potential range of 0.4 V ~ -1.0 V *vs*. RHE with a scan rate of 200 mV s^{-1} for about 100 cycles. Linear cyclic voltammetry (LSV) curves were collected in 1 M KOH with or without 0.1 M KNO_3 with a scan rate of 10 mV

s^{-1}. All electrochemical experimental results have been repeated at least three times, and the final results are the average value of repeated experiments.

Nitrate electrolysis in membrane electrode assembly (MEA) system: A commercial MEA electrolyzer was applied to assess the electrochemical performance of nitrate reduction to ammonia. The nitrate electrolysis MEA system was composed of an anode, a cathode, and an anion membrane. Carbon fiber paper coated with Cu_2O@CoO yolk-shell nanocubes and commercial IrO_2 acted as anode and cathode, respectively. The anion membrane (Fumasep FAA-3-PK-130) separates the cathode and anode. 2 mg electrocatalysts and 0.3 mg carbon black were dispersed in 0.5 mL ethanol, added with 10 μL 5 wt.% Nafion solution. The uniform electrocatalyst ink was obtained after vigorously sonicated treatment for at least 30 min, and coating on the carbon fiber paper (1 cm×1 cm) by spraying method with an airbrush.

Determination of products: The quantification of NH_4^+ contents was adopted by the indophenol blue method with modification.[41] Specifically, 30 mL of electrolyte after the nitrate reduction reaction was removed from the H-cell cathodic side. Then, 2 mL of 1 M NaOH containing 5 wt.% salicylic acid and 5 wt.% sodium citrate, 100 μL of NaClO (available chlorine 4.0 wt%), and 200 μL of 1 wt.% $C_5FeN_6Na_2O$ (sodium nitroferricyanide) added into 4 mL of diluted electrolyte/standard electrolyte containing various concentrations of NH_4^+ in sequences. Keeping at ambient conduction for 2 h, the ultraviolet-visible (UV-Vis) adsorption spectroscopy was carried out to collect the absorption spectra. The formed indophenol blue appeared at a wavelength of ~665 nm. A series of standard solutions with different NH_4Cl concentrations was implemented to calibrate the concentration-absorbance curves. The contents of the initial NO_3^- and generated NO_2^- were quantified by ion chromatography (Metrohm, 930 Compact IC Flex).

The Faradaic efficiency (FE) of the liquid products were calculated by:

$$FE(\%) = \frac{Q_{pro}}{Q_{pro}} \times 100\% = \frac{n_{pro} \times N \times F \times 100\%}{j \times t} \qquad (1)$$

where n_{pro} is the amount of the liquid product in a certain volume of catholyte, t refers to the measurement time at the applied negative potential, N is the number of electrons transferred to produce 1 mol of the liquid product, F represents to the Faradaic constant with the value of 96485 C mol^{-1}, and j is the current density at an applied negative potential.

The yield rate (μg_{NH3} h^{-1} cm^{-2}) of ammonia was calculated as follows:

$$Yield\ rate\ (NH_3) = \frac{C_{NH_3} \times V}{t \times A} \qquad (2)$$

The C_{NH3} refers to the molarity of NH_3 product, V is the volume of electrolyte, t represents to the measurement time, A means the area of the carbon fiber paper of loaded electrocatalysts (1 cm×1 cm).

Kinetic evaluation: The rate constants of electrochemical NO_3^- reduction (k_1) and electrochemical NO_2^- reduction (k_2) were conducted at -0.3 V *vs*. RHE in 1 M KOH +0.1 KNO_3 or 0.1 M KNO_2, respectively. Supposing the concentrations of NO_3^- or NO_2^- declined exponentially as per first-order rate, the rate constants (k_1 or k_2) were calculated by plotting the concentration of NO_3^- or NO_2^- against the time of reaction.

$C_t = C_{0\ exp}(-k \times t)$

While C_0 the initial concentration of NO_3^- or NO_2^- (g mL^{-1}), C_0 refers to the concentration of NO_3^- of NO_2^- at time t (g mL^{-1}), t is the time of reaction (min).

***In situ* Raman measurements**: The *in situ* Raman spectroscopy measurements were performed in a customized cell. The carbon fiber paper loaded with Cu_2O@CoO yolk-shell nanocubes served as the working electrode. An Ag/AgCl electrode and Pt wire were used as reference electrode and counter electrode, respectively. The anion membrane (Fumasep FAA-3-PK-130) separated the

cathode and the anode. We adopted a long-focus objective (8mm) of A×50 magnification for protecting the objective from corrosion. Cyclic voltammetry measurement was carried out at a scan rate of 0.2 mV s^{-1}. For *in situ* Raman spectrum recorded during the chronoamperometric test, each spectrum was collected after 6 min electrolysis with a collection time of ~40 s.

Structural characterizations: Scanning electron microtron (SEM) images were carried out on a field-emission SEM (JEOL JSM-7600F). Transmission electron microscope (TEM), high-resolution TEM, SEAD patterns, and mapping images were collected on a TEM (JEOL JEM 2010UHR) at an accelerating voltage of 200 kV. XRD patterns were carried out on a Bruke D8 Advance X-ray diffractometer equipped with a Cu Kα X-ray source (λ=1.5406 Å). XPS spectra were collected by an SSI S-Probe XPS spectrometer and calibrated using the C 1s peak at 248.8 eV.

ASSOCIATED CONTENT

Supporting Information.

The following files are available free of charge.

Additional figures and tables as described in the text (PDF)

AUTHOR INFORMATION

Corresponding Author

Bin Liu ― Department of Materials Science and Engineering, City University of Hong Kong, Hong Kong SAR 999077, China; Email: bliu48@cityu.edu.hk (B.L.)

Qingyu Yan ― School of Materials Science and Engineering, Nanyang Technological University, Singapore 639798, Singapore; Email: alexyan@ntu.edu.sg (Q.Y.)

Notes

The authors declare no competing financial interest.

Author Contributions

W.H., B.L., and Q.Y. conceived and designed the project. W.H. conducted the experimental and material characterizations. W.H., B.L., and Q.Y. wrote this paper, and all authors contributed to discussing and revising the paper.

ACKNOWLEDGMENT

The authors acknowledge funding support from Singapore MOE AcRF Tier 1 grant RT6/22, MTC programmatic fund (Grant No. 23L9b0052) from A*STAR, and the City University of Hong Kong Startup fund.

REFERENCES

[1] Wang, Y., Wang, C., Li, M., Yu, Y., Zhang, B. Nitrate Electroreduction: Mechanism Insight, *in Situ* Characterization, Performance Evaluation, and Challenges. *Chem. Soc. Rev.* **2021**, *50*, 6720-6733.

[2] Xu, H., Ma, Y., Chen, J., Zhang, W.-X., Yang, J. Electrocatalytic Reduction of Nitrate–A Step Towards a Sustainable Nitrogen Cycle. *Chem. Soc. Rev.* **2022**, *51*, 2710-2758.

[3] Suryanto, B.H.R., Du, H.-L., Wang, D., Chen, J., Simonov, A.N., MacFarlane, D.R. Challenges and Prospects in the Catalysis of Electroreduction of Nitrogen to Ammonia. *Nat. Catal.* **2019**, *2*, 290-296.

[4] Soloveichik, G. Electrochemical Synthesis of Ammonia As a Potential Alternative to the Haber–Bosch Process. *Nat. Catal.* **2019**, *2*, 377-380.

[5] Lv, F., Sun, M., Hu, Y., Xu, J., Huang, W., Han, N., Huang, B., Li, Y. Near-Unity Electrochemical Conversion of Nitrate to Ammonia on Crystalline Nickel Porphyrin-Based Covalent Organic Frameworks. *Energy Environ. Sci.* **2023**, *16*, 201-209.

[6] Cheng, H., Cui, P., Wang, F., Ding, L.X., Wang, H. High Efficiency Electrochemical Nitrogen Fixation Achieved with a Lower Pressure Reaction System by Changing the Chemical Equilibrium. *Angew. Chem., Int. Ed.* **2019**, *131*, 15687-15693.

[7] Du, H.-L., Matuszek, K., Hodgetts, R.Y., Ngoc Dinh, K., Cherepanov, P.V., Bakker, J.M., MacFarlane, D.R., Simonov, A.N. The Chemistry of Proton Carriers in High-Performance Lithium-Mediated Ammonia Electrosynthesis. *Energy Environ. Sci.* **2023**, *16*, 1082-1090.

[8] Li, P., Liao, L., Fang, Z., Su, G., Jin, Z., Yu, G. A Multifunctional Copper Single-Atom Electrocatalyst Aerogel for Smart Sensing and Producing Ammonia From Nitrate. *Proc. Natl. Acad. Sci.* **2023**, *120*, e2305489120.

[9] Wei, X., Chen, C., Fu, X.-Z., Wang, S. Oxygen Vacancies-Rich Metal Oxide for Electrocatalytic Nitrogen Cycle. *Adv. Energy Mater.* **2023**, *13*, 2303027.

[10] Chen, G.-F., Yuan, Y., Jiang, H., Ren, S.-Y., Ding, L.-X., Ma, L., Wu, T., Lu, J., Wang, H. Electrochemical Reduction of Nitrate to Ammonia *via* Direct Eight-Electron Transfer Using a Copper–Molecular Solid Catalyst. *Nat. Energy* **2020**, *5*, 605-613.

[11] Liang, J., Li, Z., Zhang, L., He, X., Luo, Y., Zheng, D., Wang, Y., Li, T., Yan, H., Ying, B., Sun, S., Liu, Q., Hamdy, M.S., Tang, B., Sun, X. Advances in Ammonia Electrosynthesis from Ambient Nitrate/Nitrite Reduction. *Chem* **2023**, *9*, 1768-1827.

[12] Song, W., Yue, L., Fan, X., Luo, Y., Ying, B., Sun, S., Zheng, D., Liu, Q., Hamdy, M.S., Sun, X. Recent Progress and Strategies on Design of Catalysts for Electrochemical Ammonia Synthesis from Nitrate Reduction. *Inorg. Chem. Front.* **2023**, *10*, 3489-3514.

[13] van Langevelde, P.H., Katsounaros, I., Koper, M.T. Electrocatalytic Nitrate Reduction for Sustainable Ammonia Production. *Joule* **2021**, *5*, 290-294.

[14] Zhang, H., Wang, H., Cao, X., Chen, M., Liu, Y., Zhou, Y., Huang, M., Xia, L., Wang, Y., Li, T., Zheng, D., Luo, Y., Sun, S., Zhao, X., Sun, X. Unveiling Cutting-Edge Developments in Electrocatalytic Nitrate-to-Ammonia Conversion. *Adv. Mater.* **2024**, *36*, 2312746.

[15] Zhao, Y., Shi, X., Ong, S.J.H., Yao, Q., Chen, B., Hou, K., Liu, C., Xu, Z.J., Guan, L. Enhancing the Charge Transportation Ability of Yolk–Shell Structure for High-Rate Sodium and Potassium Storage. *ACS Nano* **2020**, *14*, 4463-4474.

[16] Zorlu, T., Becerril‐Castro, I.B., Puertolas, B., Giannini, V., Correa‐Duarte, M.A., Alvarez‐Puebla, R.A. Yolk‐Shell Nanostars@Metal Ormganic Frameworks As Molecular Sieves for Optical Sensing and Catalysis. *Angew. Chem., Int. Ed.* **2023**, *135*, e202305299.

[17] Yang, M., Zhang, C.H., Li, N.W., Luan, D., Yu, L., Lou, X.W. Design and Synthesis of Hollow Nanostructures for Electrochemical Water Splitting. *Adv. Sci.* **2022**, *9*, 2105135.

[18] Purbia, R., Paria, S. Yolk/Shell Nanoparticles: Classifications, Synthesis, Properties, and Applications. *Nanoscale* **2015**, *7*, 19789-19873.

[19] He, W., Zhang, J., Dieckhöfer, S., Varhade, S., Brix, A.C., Lielpetere, A., Seisel, S., Junqueira, J.R.C., Schuhmann, W. Splicing the Active Phases of Copper/Cobalt-Based Catalysts Achieves High-Rate Tandem Electroreduction of Nitrate to Ammonia. *Nat. Commun.* **2022**, *13*, 1129.

[20] Zhang, J., He, W., Quast, T., Junqueira, J.R.C., Saddeler, S., Schulz, S., Schuhmann, W. Single-entity Electrochemistry Unveils Dynamic Transformation during Tandem Catalysis of Cu_2O and Co_3O_4 for Converting NO_3^- to NH_3. *Angew. Chem., Int. Ed.* **2023**, *62*, e202214830.

[21] Zhang, X., Wang, Y., Liu, C., Yu, Y., Lu, S., Zhang, B. Recent Advances in Non-Noble Metal Electrocatalysts for Nitrate Reduction. *Chem. Eng. J.* **2021**, *403*, 126269.

[22] Chen, J., He, X., Li, J., Li, X., Cai, Z., Luo, Y., Zheng, D., Li, T., Wang, Y., Liu, Q. Three-Dimensional Porous Co Foam with Nanosheets Subunits for High-Performance Electrocatalytic Nitrate-to-Ammonia Conversion. *Inorg. Chem. Front.* **2023**, *10*, 4450-4455.

[23] Fang, J.-Y., Zheng, Q.-Z., Lou, Y.-Y., Zhao, K.-M., Hu, S.-N., Li, G., Akdim, O., Huang, X.-Y., Sun, S.-G. Ampere-Level Current Density Ammonia Electrochemical Synthesis Using CuCo Nanosheets Simulating Nitrite Reductase Bifunctional Nature. *Nat. Commun.* **2022**, *13*, 7899.

[24] Fan, X., Zhao, D., Deng, Z., Zhang, L., Li, J., Li, Z., Sun, S., Luo, Y., Zheng, D., Wang, Y., Ying, B., Zhang, J., Alshehri, A.A., Lin, Y., Tang, C., Sun, X., Zheng, Y. Constructing

Co@TiO_2 Nanoarray Heterostructure with Schottky Contact for Selective Electrocatalytic Nitrate Reduction to Ammonia. *Small* **2023**, *19*, 2208036.

[25] Liu, X., Liu, C., He, X., Cai, Z., Dong, K., Li, J., Fan, X., Xie, T., Yang, X., Luo, Y., Zheng, D., Sun, S., Alfaifi, S., Gong, F., Sun, X. Fe-Doped Co_3O_4 Nanowire Strutted 3D Pinewood-Derived Carbon: A Highly Selective Electrocatalyst for Ammonia Production via Nitrate Reduction. *Nano Res.* **2024**, *17*, 2276-2282.

[26] Nai, J., Tian, Y., Guan, X., Guo, L. Pearson's Principle Inspired Generalized Strategy for the Fabrication of Metal Hydroxide and Oxide Nanocages. *J. Am. Chem. Soc.* **2013**, *135*, 16082-16091.

[27] Petitto, S., Langell, M. Surface Composition and Structure of Co_3O_4 (110) and The Effect of Impurity Segregation. *J. Vac. Sci. Technol., A* **2004**, *22*, 1690-1696.

[28] Liu, X., Xu, M., Ma, J., Zhang, X., Luan, C., Feng, X., Song, A. Cu_2O Epitaxial Films with Domain Structures Prepared on Y-Tsabilized ZrO_2 Usbstrates by Pulsed Laser Deposition. *Ceram. Int.* **2017**, *43*, 15500-15504.

[29] Guan, Q., Cheng, J., Li, X., Wang, B., Huang, L., Nie, F., Ni, W. Low Temperature Vacuum Synthesis of Triangular CoO Nanocrystal/Graphene Nanosheets Composites with Enhanced Lithium Storage Capacity. *Sci. Rep.* **2015**, *5*, 10017.

[30] Choi, H.C., Jung, Y.M., Noda, I., Kim, S.B. A Study of the Mechanism of the Electrochemical Reaction of Lithium with CoO by Two-Dimensional Soft X-Ray Absorption

Spectroscopy (2D XAS), 2D Raman, and 2D Heterospectral XAS−Raman Correlation Analysis. *J. Phys. Chem. B* **2003**, *107*, 5806-5811.

[31] Lee, W.H., Han, M.H., Ko, Y.-J., Min, B.K., Chae, K.H., Oh, H.-S. Electrode Reconstruction Strategy for Oxygen Evolution Reaction: Maintaining Fe-CoOOH Phase with Intermediate-Spin State During Electrolysis. *Nat. Commun.* **2022**, *13*, 605.

[32] Liu, H., Guo, D., Zhang, W., Cao, R. $Co(OH)_2$ Hollow Nanoflowers as Highly Efficient Electrocatalysts for Oxygen Evolution Reaction. *J. Mater. Res.* **2017**, *33*, 568-580.

[33] Wang, Y., Xu, A., Wang, Z., Huang, L., Li, J., Li, F., Wicks, J., Luo, M., Nam, D.-H., Tan, C.-S., Ding, Y., Wu, J., Lum, Y., Dinh, C.-T., Sinton, D., Zheng, G., Sargent, E.H. Enhanced Nitrate-to-Ammonia Activity on Copper–Nickel Alloys *via* Tuning of Intermediate Adsorption. *J. Am. Chem. Soc.* **2020**, *142*, 5702-5708.

[34] Liu, J.-X., Richards, D., Singh, N., Goldsmith, B.R. Activity and Selectivity Trends in Electrocatalytic Nitrate Reduction on Transition Metals. *ACS Catal.* **2019**, *9*, 7052-7064.

[35] Liu, Y., Wei, J., Yang, Z., Zheng, L., Zhao, J., Song, Z., Zhou, Y., Cheng, J., Meng, J., Geng, Z., Zeng, J. Efficient Tandem Electroreduction of Nitrate into Ammonia Through Coupling Cu Single Atoms with Adjacent Co_3O_4. *Nat. Commun.* **2024**, *15*, 3619.

[36] Li, Y., Go, Y.K., Ooka, H., He, D., Jin, F., Kim, S.H., Nakamura, R. Enzyme Mimetic Active Intermediates for Nitrate Reduction in Neutral Aqueous Media. *Angew. Chem., Int. Ed.* **2020**, *59*, 9744-9750.

[37] Dima, G.E., de Vooys, A.C.A., Koper, M.T.M. Electrocatalytic Reduction of Nitrate at Low Concentration on Coinage and Transition-Metal Electrodes in Acid Solutions. *J. Electroanal. Chem.* **2003**, *554*, 15-23.

[38] Lefebvre, M.C., Establishing the Link Between Multistep Electrochemical Reaction Mechanisms and Experimental Tafel Slopes, in: Mod. Aspects Electrochem., Springer, 2002, pp. 249-300.

[39] Fang, Y.-H., Liu, Z.-P. Tafel Kinetics of Electrocatalytic Reactions: From Experiment to First-Principles. *ACS Catal.* **2014**, *4*, 4364-4376.

[40] Petrii, O.A., Nazmutdinov, R.R., Bronshtein, M.D., Tsirlina, G.A. Life of the Tafel Equation: Current Understanding and Prospects for the Second Century. *Electrochim. Acta* **2007**, *52*, 3493-3504.

[41] Zhu, D., Zhang, L., Ruther, R.E., Hamers, R.J. Photo-Illuminated Diamond as a Solid-State Source of Solvated Electrons in Water for Nitrogen Reduction. *Nat. Mater.* **2013**, *12*, 836-841.

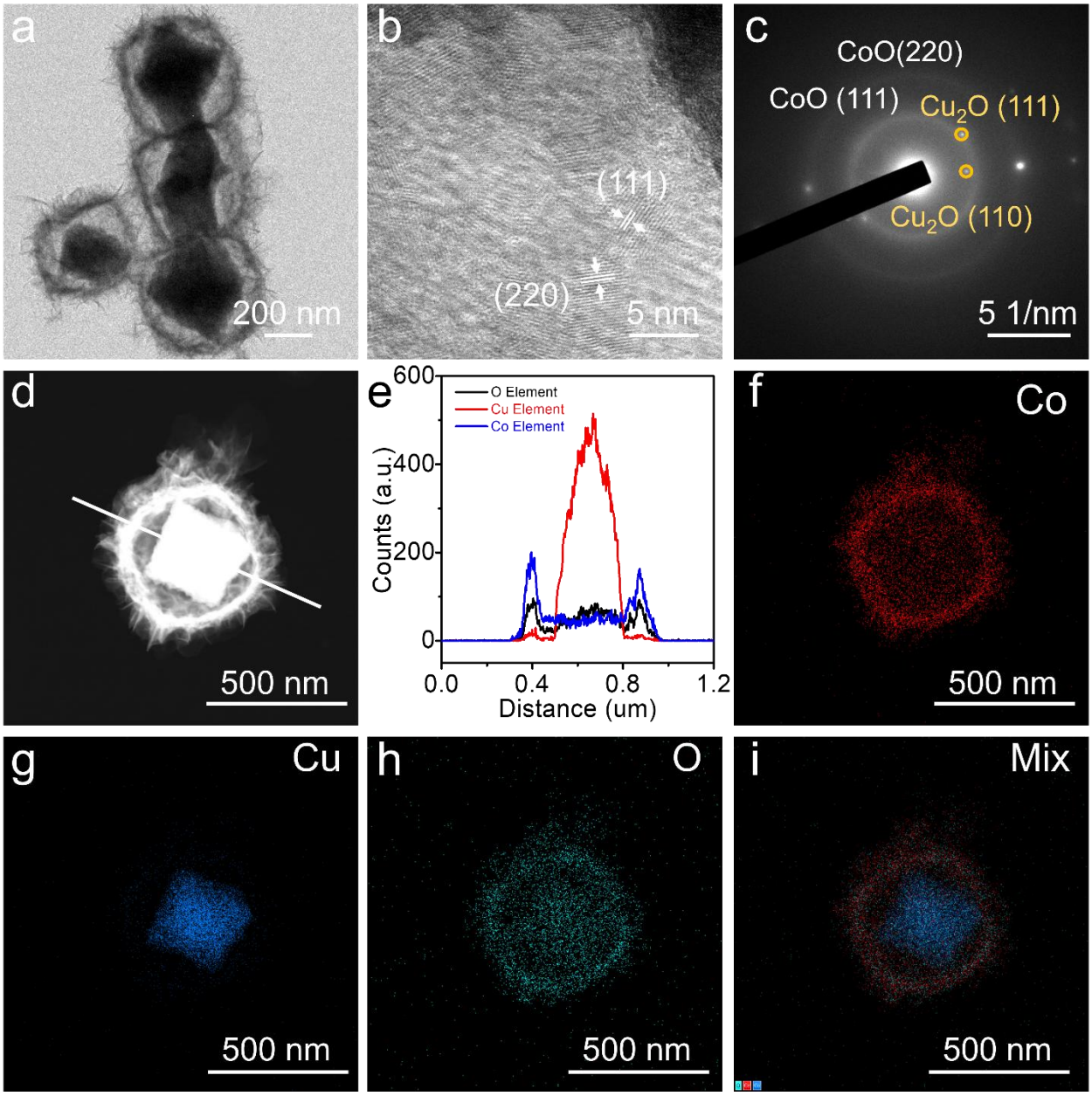


Figure 1. Structure characterizations of Cu_2O@CoO yolk-shell nanocubes. (a, b) TEM and HR-TEM images of Cu_2O@CoO yolk-shell nanocubes. (c) Selected area electron diffraction (SAED) pattern of Cu_2O@CoO yolk-shell nanocubes. (d) High-angle annular dark-field scanning transmission electron microscopy (HADDF-STEM) image of a Cu_2O@CoO yolk-shell nanocube and (e) the corresponding energy-dispersive X-ray spectroscopy (EDS) line scan profiles. (f-i) The corresponding EDS elemental mapping images.

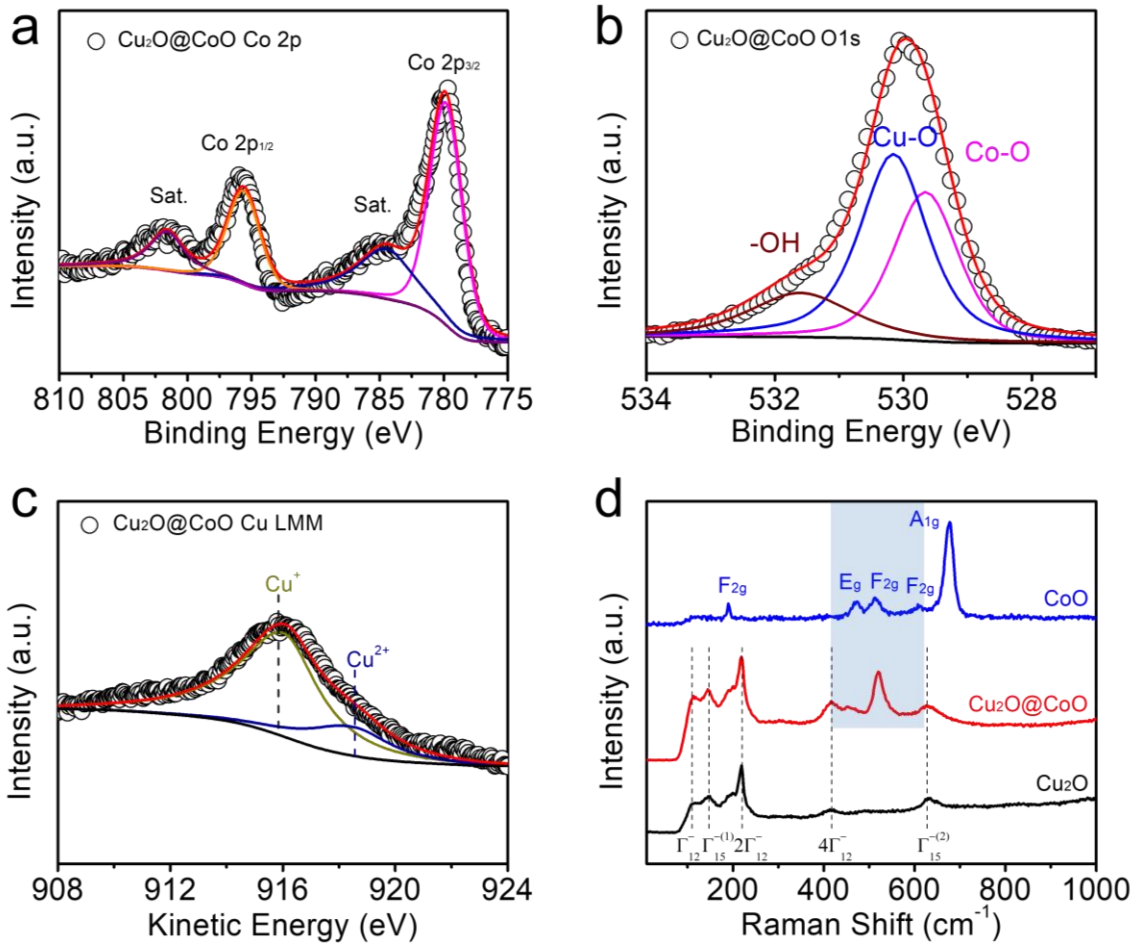


Figure 2. X-ray photoelectron spectroscopy and Raman spectroscopy analysis. High-resolution (a) Co 2p, (b) O 1s and (c) The fitted Cu LMM XPS spectrum of Cu_2O@CoO yolk-shell nanocubes. (d) Raman spectra of Cu_2O nanocubes, CoO nanosheets, and Cu_2O@CoO yolk-shell nanocubes.

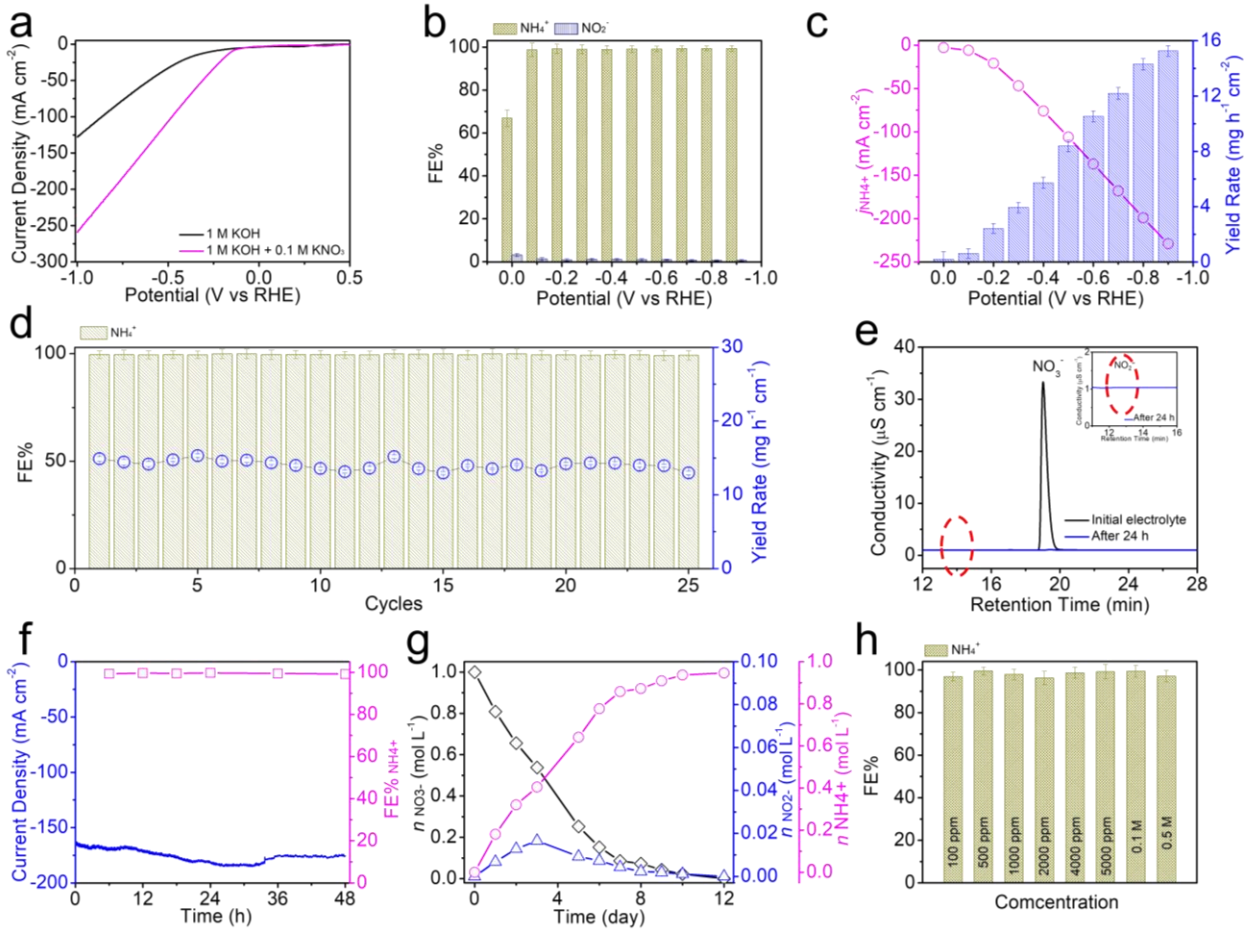


Figure 3. Electrocatalytic NO_3^-RR performance. (a) Linear sweep voltammetry (LSV) curves of Cu_2O@CoO yolk-shell nanocubes recorded in 1 M KOH with and without 0.1 M KNO_3. (b) Potential-dependent Faradaic efficiency of NH_4^+ and NO_2^- over Cu_2O@CoO yolk-shell nanocubes. (c) The NH_4^+ partial current density and NH_4^+ yield rate over Cu_2O@CoO yolk-shell nanocubes at the potential range from 0 to -0.9 V *vs*. RHE. (d) Consecutive cycling measurements at -0.8 V *vs*. RHE on Cu_2O@CoO yolk-shell nanocubes with corresponding NH_4^+ Faradaic efficiency and yield rate. (e) The IC curves of fresh 1 M KOH + 0.1 M KNO_3 electrolyte and 1 M KOH + 0.1 M KNO_3 electrolyte after 24 h of nitrate reduction reaction over Cu_2O@CoO yolk-shell nanocubes at -0.4 V *vs*. RHE. Inset shows the enlarged NO_2^- signal region after 24 h. The NO_2^- and NO_3^- peaks are located at the retention time of 12.63 min and 19.05 min, respectively. Both electrolytes

were diluted 100 times. (f) Long-time stability measurement of Cu_2O@CoO yolk-shell nanocubes at -0.8 V *vs*. RHE. (g) The concentration evolution of NO_3^-, NO_2^- and NH_4^+ over time. (h) Potential-dependent Faradaic efficiency (FE) of NH_4^+ over Cu_2O@CoO yolk-shell nanocubes in 1 M KOH with various concentrations of NO_3^-.

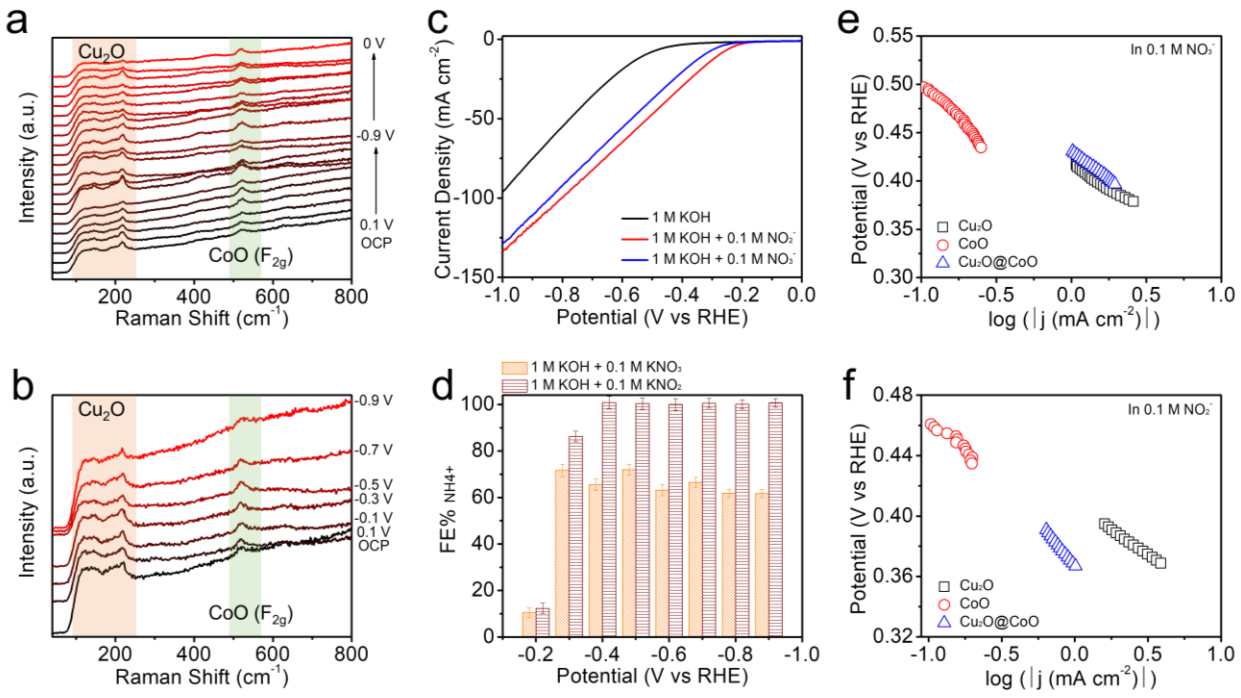


Figure 4. *In-situ* Raman measurements and cascade electrochemical mechanism exploration. (a) *In-situ* Raman spectra of Cu_2O@CoO yolk-shell nanocubes recorded during CV measurement at OCP and the applied potential window of 0.1 V ~ -0.9 V *vs*. RHE in 0.01 M KNO_3 + 0.01 M KOH + 0.04 M K_2SO_4. (b) *In-situ* Raman spectra of Cu_2O@CoO yolk-shell nanocubes recorded after applying a constant potential for 6 min at OCP and the applied negative potential window of 0.1 V ~ -0.9 V *vs*. RHE in 0.01 M KNO_3 + 0.01 M KOH + 0.04 M K_2SO_4. Fast cyclic voltammetry scans were carried out for electrocatalyst activation before *in-situ* Raman measurement. (c) Linear sweep voltammetry (LSV) curves of CoO nanosheets recorded in 1 M KOH, 1 M KOH + 0.1 M KNO_2, and 1 M KOH + 0.1 M KNO_3. (d) Potential-dependent Faradaic efficiency of NH_4^+ over CoO nanosheets in 1 M KOH + 0.1 M KNO_3 and 1 M KOH + 0.1 M KNO_2. (e) Tafel plots of Cu_2O nanocubes, CoO nanosheets and Cu_2O@CoO yolk-shell nanocubes in 1 M KOH + 0.1 M KNO_3. (f) Tafel plots of Cu_2O nanocubes, CoO nanosheets and Cu_2O@CoO yolk-shell nanocubes in 1 M KOH + 0.1 M KNO_2.

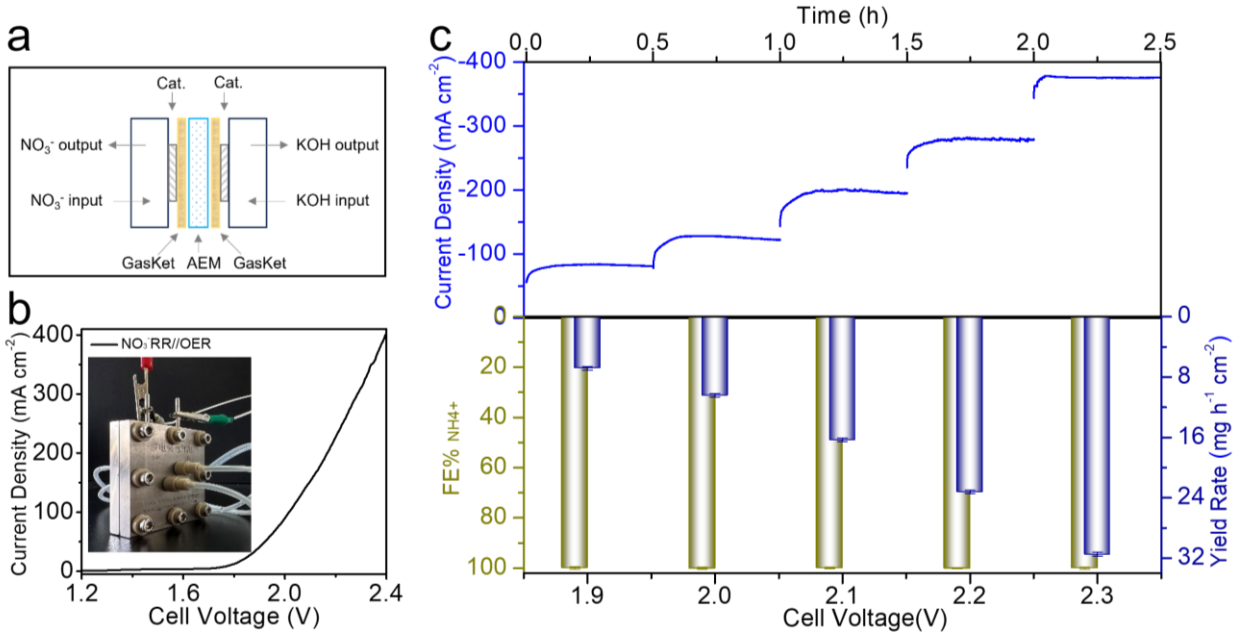


Figure 5. Electrochemical performances of MEA. (a) Schematic diagram showing the MEA nitrate electrolysis cell. (b) Polarization curve of the MEA nitrate electrolysis cell with a Cu_2O@CoO yolk-shell nanocube cathode and an IrO_2 anode. Inset shows a photograph of the MEA electrolysis cell. (c) The i-t curves of the MEA nitrate electrolysis cell with a Cu_2O@CoO yolk-shell nanocube cathode and an IrO_2 anode collected in the cell voltage window from 1.9 to 2.3 V and the corresponding NH_4^+ Faradaic efficiency and yield rate.

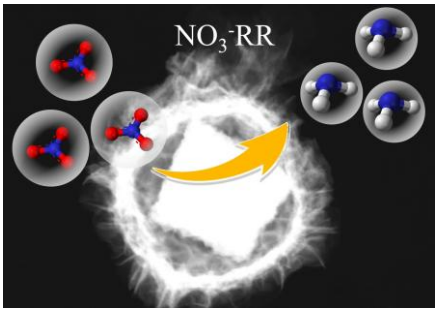


Table of the Content

In this work, we explored the well-defined special hierarchical structures with various active species for highly efficient electrochemical nitrate reduction to ammonia. Cu_2O@CoO yolk-shell nanocubes possessed > 99 % NH_4^+ FE in a potential window of -0.2 ~ -0.9 V vs. RHE, and over 90% NO_3^--N to NH_4^+-N conversion efficiency in diluted (500 ppm) and concentrated (0.1 M and 1 M) NO_3^- electrolytes. The great electrochemical performance of Cu_2O@CoO originated from the efficient cascade synergetic promotion role of their hierarchical structure and reasonable chemical composition.